Phys Chem Minerals
DOI 10.1007/s00269-015-0738-9

ORIGINAL PAPER

Structural and magnetic phase transitions in the synthetic clinopyroxene $LiCrGe_2O_6$: a neutron diffraction study between 0.5 and 1473 K

Günther J. Redhammer · Anatoliy Senyshyn · Gerold Tippelt · Sebastian Prinz · Georg Roth

Received: 10 November 2014 / Accepted: 12 February 2015

Abstract The pyroxene-type compound $LiCrGe_2O_6$, the Li- and Ge-analogue to the silicate mineral kosmochlor, has been synthesized at 1373 K and investigated by neutron diffraction between 0.5 and 1473 K in order to investigate the variation in magnetic and crystal structure with temperature. A structural phase transition from a low-temperature $P2_1/c$ to a high-temperature $C2/c$ structure was found around 1140 K. The two different structures exhibit different thermal expansion behavior with temperature with a reversal of the largest thermal expansion from the **c**-axis to the **b**-axis in the $P2_1/c$ and $C2/c$ phase, respectively. The structural phase transition is accompanied by a large volume increase of 1.9 % and sharp discontinuities in bond lengths, especially for the Li–O and—to a lesser extent—for the Cr–O bonds. At low temperature, some additional nonlinear changes in lattice parameters occur, which are associated with a magnetoelastic couplings of the lattice. Magnetic ordering is observed below 6 K in the neutron diffraction data. Data could be indexed with $\boldsymbol{k} = (0\ 0\ 0)$, giving rise to magnetic space group $P2_1'/c$. This model of the magnetic structure has a pure antiferromagnetic arrangement of spins, both within and between the M1 chains. The spins are oriented within the **a**–**c** plane with an almost nil component along [0 1 0]. A shift of the Cr atom out of the center in the equatorial plane of the octahedron is observed below 6 K and is associated with the magnetic phase transition.

Keywords $LiCrGe_2O_6$ · Pyroxene · Neutron diffraction · Structural phase transition · Magnetic phase transition

Introduction

The mineral group of the pyroxenes has a rich crystal chemistry, and especially the Li-bearing clinopyroxenes show phase transitions as a function of temperature (Cámara et al. 2003a, b, 2009; Redhammer et al. 2001, 2003; Redhammer and Roth 2004a, b; Redhammer et al. 2010a, b; Tribaudino et al. 2002, 2003, 2009) and pressure (e.g., Nestola et al. 2008, 2009). It is well understood that silicate $LiM^{3+}Si_2O_6$ clinopyroxenes (M = Fe, Cr, Ga, V, and Sc) transform from a low-temperature $P2_1/c$ to a high-temperature HT-$C2/c$ structure between ~200 and 360 K depending on chemistry (Redhammer and Roth 2004a; Cámara et al. 2009). Recently, Redhammer et al. (2010b) investigated the temperature evolution of the synthetic clinopyroxene $LiFeGe_2O_6$ and found the $P2_1/c \Leftrightarrow$ HT-$C2/c$ phase transition temperature shifted by almost 560 K toward higher temperatures as compared with the analogue silicate (Redhammer et al. 2001). The structural phase transition in the germanate is associated with a sharp discontinuity of the lattice parameters, causing the single crystals to frequently break during data collection. Thus, only few

Electronic supplementary material The online version of this article (doi:10.1007/s00269-015-0738-9) contains supplementary material, which is available to authorized users.

G. J. Redhammer (✉) · G. Tippelt
Division of Mineralogy, Department of Materials Science and Physics, University of Salzburg, Hellbrunnerstr. 34, 5020 Salzburg, Austria
e-mail: Guenther.Redhammer@Sbg.ac.At

A. Senyshyn
Maier-Leibnitz-Zentrum (MLZ), Technical University Munich, Lichtenbergstrasse 1, 85747 Garching, Germany

S. Prinz · G. Roth
Institute of Crystallography, RWTH Aachen University, Jägerstraße 17/19, 52056 Aachen, Germany

Published online: 24 February 2015

data points could be collected in the HT-$C2/c$ phase using single-crystal X-ray diffraction in $LiFeGe_2O_6$. Additionally, large anisotropic atomic displacements for Li^+ were observed in $LiFeGe_2O_6$ at higher temperatures. Because the pyroxene $LiCrGe_2O_6$ also shows $P2_1/c$ symmetry at room temperature (Redhammer et al. 2009a), it is obvious to seek for the $P2_1/c \Leftrightarrow$ HT-$C2/c$ phase transition in this compound also; this time using high-resolution powder neutron diffraction data.

Not only the structural, but also the magnetic phase transitions at low temperatures make the pyroxenes an attractive group of materials. Jodlauk et al. (2007) found multiferroic/magnetoelectric behavior in the pyroxenes $NaFeSi_2O_6$, $LiFeSi_2O_6$, and $LiCrSi_2O_6$, initiating an increased interest of solid-state physicists in this mineral group. The specific structural topology of the pyroxenes with their infinite quasi-1D chains of transition-metal-bearing octahedral M1 sites and their linkage via the infinite chains of corner-sharing TO_4 tetrahedra and the approximately triangular lattice for magnetic superexchange pathways together cause a pattern of competing magnetic exchange interactions, which eventually lead to frustration and a variety of competing magnetically ordered ground states. Depending on the dominating interaction, either within or between the M1 chains, this finally determines the bulk magnetic properties. In a series of papers (Redhammer et al. 2001, 2008, 2009b, 2010a, 2011a, b, 2012, 2013), we were able to show that even small structural alterations in chemically similar systems can cause transformation into distinctly different magnetically ordered states. Typical systems therefore are the four-component system $(Na,Li)Fe^{3+}(Si,Ge)_2O_6$ (Redhammer et al. 2001, 2009b, 2010a) or $(Na,Li)Cr^{3+}(Si,Ge)_2O_6$ (Nenert et al. 2009a, b, 2010a, b; Streltsov and Khomskii 2008). To our understanding, the following ingredients contribute to the diversity of magnetic ground states in pyroxenes: Almost 90° M1–O–M1 superexchange coupling between the edge sharing M1 octahedra within the octahedral chain with a resulting ambiguity of even the sign of the strongest intra-chain interaction, the competing superexchange interaction via one or two (depending on symmetry) different kinds of $(Si,Ge)O_4$—tetrahedra, and an intrinsic structural instability toward the kinking of the tetrahedral chains, which in turn modulates the superexchange interaction in a more subtle way. Besides the structural phase transition at high temperature, this study also intends to investigate the magnetic properties of $LiCrGe_2O_6$ at very low temperatures ($T < 3$ K), also not reported in the literature so far.

The nuclear structure of $LiCrGe_2O_6$ was first reported by Redhammer et al. (2009a) using single-crystal X-ray data at room temperature, undoubtedly yielding the $P2_1/c$ space group. At almost the same time, Matsushita et al. (2010) extracted structural data on $LiCrGe_2O_6$ from X-ray powder diffraction data, but falsely determined the space group to be $C2/c$ and gave unrealistic bond lengths and angles, especially for the tetrahedral sites. Also, Janson et al. (2014) expressed their doubts about the true symmetry of $LiCrGe_2O_6$, whether being $C2/c$ or $P2_1/c$ at 298 K, even if they index the low-temperature neutron data in space group $P2_1/c$. During the course of this study, the magnetic structure of $LiCrGe_2O_6$ was determined recently by Nenert et al. (2010b) using 1.7 K powder neutron diffraction data, finding magnetic space group $P2_1'/c$ and yielding a structure with antiferromagnetically coupled spins within the M1 chains and ferromagnetic coupling between the chains. In a very recent work, Janson et al. (2014) studied magnetoelectric $LiCrSi_2O_6$ and $LiCrGe_2O_6$ by means of density functional theory (DFT) calculations, quantum Monte Carlo simulations (QMC), neutron diffraction at 1.7 K, and high-field magnetization measurements. They found that the magnetic interaction in $LiCrGe_2O_6$ is constituted by three different exchange couplings, with the leading coupling being between the M1 chains, followed by the exchange coupling within the M1 chain, and the second inter-chain coupling, which is two times smaller than the latter one (Janson et al. 2014). In the present study, we will report on both magnetic and the nuclear phase transitions in $LiCrGe_2O_6$ and follow the thermal evolution of the magnetic and nuclear structure in a large temperature range between 0.5 and 1473 K.

Experimental

Synthesis and preliminary sample characterization

A polycrystalline sample of $LiCrGe_2O_6$ was prepared by a solid-state ceramic sintering route using Li_2CO_3, Cr_2O_3, and GeO_2 in the exact stoichiometry of the compound as starting materials. Chemicals were finely ground under ethanol, dried, pressed to pellets, and fired at 1273 K for 2–3 days in a first step using platinum crucibles and a high-temperature chamber furnace. In four following subsequent synthesis cycles, 5 days each, temperature was raised to 1373 K. The final synthesis batch was a single phase sample of $LiCrSi_2O_6$ as proved by powder X-ray diffraction and showed an emerald green color. Differential thermal analysis on a 32-mg sample using a Netzsch STA 449F3 between 298 and 1273 K, heating rate 5 K/min under Ar atmosphere, shows a well-defined peak at 1140 K (area of 21 J/g), which is assigned to the crystallographic $P2_1/c$–$C2/c$ phase transition. DTA plots can be found as supplemental information.

Neutron diffraction experiments

Neutron diffraction experiments were done at the Maier-Leibnitz-Zentrum (MLZ), FRM-II, Munich, Germany.

Table 1 Experimental details and results of Rietveld refinements of constant-wavelength neutron diffraction pattern of $LiCrGe_2O_6$ at some selected temperatures (the full set of data is deposited within the CIF)

T (K)	3	10	310	1073	1173	1473
S.G.	$P2_1/c$	$P2_1/c$	$P2_1/c$	$P2_1/c$	$C2/c$	$C2/c$
a (Å)	9.79142(9)	9.79045(9)	9.80296(9)	9.89040(9)	10.0109(2)	10.0269(15)
b (Å)	8.71562(7)	8.71647(7)	8.72305(8)	8.77364(9)	8.7497(1)	8.7863(17)
c (Å)	5.33503(5)	5.33654(5)	5.34637(5)	5.41193(5)	5.4992(1)	5.5072(9)
β (°)	108.9213(5)	108.9315(5)	108.9221(5)	108.9817(5)	110.008(11)	109.861(1)
V (Å^3)	430.681(7)	430.776(7)	432.741(7)	444.082(7)	452.612(15)	456.315(13)
R_p (%)	2.91	2.89	2.66	2.07	2.13	2.49
R_{wp} (%)	3.78	3.70	3.34	2.40	2.57	3.23
R_{exp} (%)	1.45	1.44	1.44	1.90	1.88	1.90
R_B (%)	2.69	2.77	2.68	2.11	2.22	3.63
R_{magn} (%)	5.47	–	–	–	–	–

For all data: constant-wavelength step-scan neutron data with $\lambda = 1.537$ Å, SPODI diffractometer (FRM-II, Germany) with $2\theta_{min} = 0.9°$, $2\theta_{max} = 151.9°$, stepsize = 0.04°; refinement of F^2, pseudo-Voigt function, no excluded regions

Powder diffraction data were acquired between 3 and 1473 K in constant-wavelength mode using the high-resolution powder diffractometer SPODI (Hoelzel et al. 2007) on a ~15-g batch with Ge551 monochromatized neutron radiation ($\lambda = 1.5482$ Å). Experiments were performed in a 2θ range $3° \leq 2\theta \leq 154°$, step width 0.04°, using a closed cycle cryostat with the sample contained in an Al can. The high-temperature measurements were taken with the sample contained in a V-sample holder using a vacuum high-temperature furnace. The very low-temperature measurements (0.5–10 K) were taken with a ^{3}He inset using a wavelength of 2.436 Å (Ge331 monochromator) for better resolving of the magnetic Bragg peaks. Data treatment was done using the FULLPROF suite of programs (Rodríguez-Carvajal 2001), and the structural data of Redhammer et al. (2009b) were taken as starting parameters in Rietveld refinements. Experimental data and refinement results at some selected temperatures are compiled in Table 1, fractional atomic coordinates are listed in Table 2, and some secondary structural parameters are listed in Table 3. The complete set of atomic coordinates and structural parameters, at all temperatures, is available from the crystallographic information files (CIFs), which is available as supplementary material.

Powder X-ray diffraction

Prior to the neutron diffraction experiments, step-scan powder X-ray diffraction data (10°–100° in 2Θ, continuous scan) were collected in the temperature range 300–1273 K, on a Philips X'Pert diffractometer (CuK_α radiation, fixed 0.125° divergence slit, primary and secondary 0.04 rad Soller slits, conventional point detector, Anton Parr HTK-16 high-temperature chamber). This was done to establish a second data basis for thermal expansion tensor/strain calculations, especially in the close vicinity of the expected $P2_1/c$–$C2/c$ phase transition.

Results and discussion

Lattice parameters and thermal expansion

The variation in unit cell parameters with temperature is shown in Fig. 1, the insets display the low-temperature region on an enhanced scale, and Table S1 gives the full set of lattice parameters. Several discontinuities and changes in slope are evident; the most prominent are discontinuities in lattice parameters at $T_{tr} = 1140$ K, which show a small hysteresis of <10 K and which are associated with a disappearance of Bragg peaks of type $h + k = 2n + 1$, indicative of the $P2_1/c$–$C2/c$ phase transition. The transition temperature, found by in situ X-ray diffraction, is in perfect agreement with the results of the DTA analysis. Besides the strong evidence from single-crystal data (Redhammer et al. 2009a), this is further proof that the space group symmetry at 298 K, given by Matsushita et al. (2010), is incorrect; indeed, the true symmetry is $P2_1/c$. At the phase transition, the **a**-axis expands by 1.11 %, the **b**-axis shrinks by 0.38 %, and the **c**-axis and the monoclinic angle β again increase by 1.42 and 0.93 %, respectively, so the most distinct alterations involve the latter two unit cell parameters. The overall increase in unit cell volume is 1.52 %. These large changes in unit cell parameters are in good agreement with what was found for $LiFeGe_2O_6$, where a similar sudden volume increase of 1.56 % occurs at the phase transition (Redhammer et al. 2010b), however, at a distinctly lower temperature of 789 K. So, even if the ionic radii of Cr^{3+} and Fe^{3+}

Table 2 Fractional atomic coordinates and equivalent isotropic atomic displacement parameters and B_{iso} (Å^2) for $LiCrGe_2O_6$ at selected temperatures, as extracted from the Rietveld refinements of neutron diffraction data

	x	*y*	*z*	B_{iso}
$T = 3$ K				
Li	0.2588(7)	0.4856(6)	0.7220(12)	0.47(8)
Cr	0.2509(3)	0.6583(3)	0.2140(5)	0.11(3)
GeA	0.04699(12)	0.34466(15)	0.2759(2)	0.020(18)
GeB	0.55463(11)	0.84214(16)	0.2288(2)	0.076(18)
O1A	−0.14323(17)	0.3341(2)	0.1738(3)	0.22(3)
O2A	0.11464(18)	0.52671(19)	0.2851(3)	0.22(3)
O3A	0.11742(17)	0.29164(17)	0.6100(3)	0.26(3)
O1B	0.36440(16)	0.8308(2)	0.1045(3)	0.09(2)
O2B	0.6317(2)	1.0058(2)	0.3891(4)	0.38(3)
O3B	0.61360(17)	0.68806(19)	0.4535(3)	−0.05(3)
$T = 10$ K				
Li	0.2587(7)	0.4861(5)	0.7225(11)	0.42(8)
Cr	0.2514(3)	0.6579(3)	0.2139(5)	0.10(3)
GeA	0.04724(12)	0.34472(14)	0.2758(2)	0.055(17)
GeB	0.55453(11)	0.84191(16)	0.2288(2)	0.105(18)
O1A	−0.14318(16)	0.3339(2)	0.1738(3)	0.18(3)
O2A	0.11482(17)	0.52704(18)	0.2851(3)	0.19(3)
O3A	0.11728(17)	0.29178(17)	0.6095(3)	0.27(3)
O1B	0.36433(16)	0.8312(2)	0.1048(3)	0.13(2)
O2B	0.63174(19)	1.0057(2)	0.3892(4)	0.40(3)
O3B	0.61343(17)	0.68795(18)	0.4529(3)	−0.02(3)
$T = 310$ K				
Li	0.2573(8)	0.4850(7)	0.7241(13)	1.33(16)
Cr	0.2512(3)	0.6595(3)	0.2128(5)	0.18(3)
GeA	0.04714(12)	0.34464(14)	0.2741(2)	0.264(17)
GeB	0.55362(11)	0.84238(16)	0.2289(2)	0.279(18)
O1A	−0.14292(16)	0.3321(2)	0.1718(3)	0.28(2)
O2A	0.11456(18)	0.5256(2)	0.2843(3)	0.85(3)
O3A	0.11652(17)	0.29048(17)	0.6072(2)	0.53(3)
O1B	0.36438(17)	0.8314(3)	0.1055(3)	0.39(2)
O2B	0.63062(19)	1.0069(2)	0.3838(4)	0.61(3)
O3B	0.61337(18)	0.68909(19)	0.4556(3)	0.45(3)
$T = 1073$ K				
Li	0.2604(17)	0.4789(9)	0.736(2)	5.15(21)
Cr	0.2513(4)	0.6606(3)	0.2210(6)	1.08(5)
GeA	0.04545(15)	0.34496(17)	0.2626(3)	1.15(3)
GeB	0.55066(15)	0.84343(19)	0.2326(3)	1.20(3)
O1A	−0.1409(2)	0.3313(3)	0.1632(4)	1.35(5)
O2A	0.1143(3)	0.5229(3)	0.2812(5)	2.78(6)
O3A	0.11457(19)	0.2854(3)	0.5897(4)	2.05(5)
O1B	0.3629(2)	0.8333(3)	0.1111(4)	1.35(4)
O2B	0.6250(3)	1.0126(3)	0.3695(5)	2.35(6)
O3B	0.6123(2)	0.7030(2)	0.4760(4)	2.19(5)
$T = 1173$ K				
Li1	0	0.2806(11)	1/4	6.56(44)
Cr1	0	0.9126(3)	1/4	1.22(7)
Ge1	0.29350(8)	0.09579(11)	0.24489(13)	1.47(3)
O1	0.10706(11)	0.08481(16)	0.13801(19)	1.59(3)
O2	0.36178(16)	0.27493(15)	0.2987(3)	3.57(5)
O3	0.36326(14)	−0.01482(17)	0.0550(2)	3.32(5)
$T = 1473$				
Li1	0	0.2767(18)	1/4	8.47(54)
Cr1	0	0.9130(6)	1/4	1.61(9)
Ge1	0.29323(14)	0.09560(19)	0.2431(2)	1.88(4)
O1	0.10718(18)	0.0854(3)	0.1375(3)	2.06(4)
O2	0.3624(3)	0.2732(3)	0.2983(5)	4.30(7)
O3	0.3627(2)	−0.0127(3)	0.0521(4)	4.18(6)

are quite similar (0.615 and 0.645 Å, respectively, Shannon and Prewitt 1969), the $P2_1/c$ structure is stable to significantly higher temperatures in the $LiCrGe_2O_6$ as compared to $LiFeGe_2O_6$. Overall, the observed pattern with decreasing **b** and increasing **a**- and **c**-axes at the phase transition is general characteristics for the $P2_1/c$–$C2/c$ phase transition in the clinopyroxenes.

Within the $C2/c$ phase of $LiCrGe_2O_6$, the cell parameters are almost linearly correlated with temperature; small deviations from linearity are observed for the **a**-axis length and the monoclinic angle. Furthermore, changes in slope mark different thermal expansion behavior of the $P2_1/c$ and $C2/c$ phases; this is most evident for the data of the **b**-axis and the monoclinic angle. For the $P2_1/c$ phase, the lattice parameters are linearly correlated with temperature between 250 and 800 K. Only along the **b**-axis, a constant thermal expansion up to the phase transition is found, while along **a**, **c** and for β, an upward deviation is observed. A low-temperature saturation, i.e., no further changes in lattice parameters with decreasing temperature as would be expected from a gradual decrease in anharmonicity, is only observed in a pronounced way in the **b**-axis data below 200 K, **a** and **c** do not reach a completely constant value. Also evident are distinct changes in lattice parameters below 40 K. These are due to magnetoelastic coupling associated with the magnetic ordering in $LiCrGe_2O_6$. Along the **a**-axis, the lattice expands toward the ordering temperature of ~7 K, the **b**- and **c**-axes contract and β also changes in a distinct way. Below 2.5 K, a further change in the slope of lattice parameter evolution as a function of temperature is evident (insets in Fig. 1). This behavior could indicate a reorientation of the spins below 2 K. Additional hints come from small changes in magnetic moments (see below).

The evolution of lattice parameters can be modeled in its simplest way using a quasi-harmonic Einstein model, which

takes into account a low-temperature "saturation" and a constant (linear) thermal expansion above a certain temperature, as described, e.g., by Knight (1996) as follows:

$$a = a_0 + \frac{C_E}{e^{(\theta_E/T)} - 1} \quad (1)$$

where a_0 is the unit cell dimension at zero Kelvin, C_E is a constant, and θ_E is the temperature above which saturation is reached and the thermal expansion can be considered to be constant.

Good fits of the lattice parameters of the $P2_1/c$ phase with this simple Einstein model are only possible for the *b*-lattice parameters in the whole temperature range between 50 and 1140 K; for *a* and *c*, acceptable fits are obtained up to 800 K (see Fig. 1), giving rise to Debye temperatures of 460(11) K, 335(7) K, 527(11) K, and 388(8) K for *a*, *b*, *c*, and β, respectively. Distinct deviations from this model are observed above 800 K, which probably are precursor effects of the subsequent high-temperature phase transition; the simple model, which works well for other pyroxenes, is not fully sufficient to describe the evolution of lattice parameters at high temperatures in $LiCrGe_2O_6$ and close to the phase transition.

The variation in temperature induces a macroscopic strain ε, the tensor components of which can be calculated from the lattice parameters at the different temperatures. In the monoclinic system, the strain ellipsoid, whose axes are the diagonal components of the tensor (Ohashi and Burnham 1973), is constrained to have two axes within the *a*–*c* plane, while the third axis is parallel to the *b*-axis. The program WIN_STRAIN 4.11 (Angel 2011) was used for strain calculations, choosing the Eulerian strain formalism with **x//a***, **y//b**, and **z//c** as the orientation of the Cartesian reference system with respect to the crystallographic axes system. For more details on the mathematical background, see, e.g., Ohashi and Burnham (1973), Schlenker et al. (1975), Schoenfield et al. (2004), or Redhammer et al. (2010a, b). Using the same formalism, the thermal expansion tensors were calculated. In order to parameterize the evolution of the unit cell parameters within the $P2_1/c$ phase, fourth- or fifth-order polynomial functions were used; for the $C2/c$ phase, second-order polynomials were sufficient. Calculations of overall strain and thermal expansion values were based on lattice parameters derived from these polynomial functions. It should be noted that the overall strain is the sum of thermal strain and the spontaneous strain of the co-elastic $P2_1/c$–$C2/c$ phase transition. The need for higher exponentials to fit the $P2_1/c$ lattice parameters originates from the contribution from spontaneous strain. Within the $P2_1/c$ phase, the largest overall strain component is ε_{33} along the **c**-axis, which shows a distinct increase toward the phase transition. The smallest overall strain (ε_{22}) is found along the **b**-axis, which, together with ε_{11}, increases only slightly toward the T_{tr}. In fact, the very same behavior is found for the thermal expansion tensor (Fig. 2); thus, we focus on the discussion of the later quantity here. The largest axial thermal expansion in the $P2_1/c$ phase is α_{33} along the **c**-axis with a distinct nonlinear increase above 700 K toward T_{tr}; the axial components α_{11} and α_{22} remain almost constant between 400 and 800 K with values of 10.2–11.6 $\times$ 10^{-6} and 7.1–7.7 $\times$ 10^{-6} K^{-1}, respectively. Above 800 K, also these axial expansion coefficients increase toward the phase transition temperature (Table 4). For the $C2/c$ phase, the situation becomes reversed: The largest axial thermal expansion is given by α_{22} along the **b**-axis (which is the smallest α_{ij} in $P2_1/c$), the smallest is given by α_{33} along the **c**-axis, which was the largest in $P2_1/c$). Both values remain constant, and only α_{11} is increasing steadily. Diagonalization of the tensor components yields the main axes of the thermal expansion ellipsoids (Fig. 2b). As α_2 is constrained to be parallel to the **b**-axis, it has the same numeric value as α_{22}; the thermal expansion along **b** thus remains the smallest one within the $P2_1/c$ phase, increases, however, close to the phase transition from ~8.8 $\times$ 10^{-6} to 13.7 $\times$ 10^{-6} K^{-1} between 1130 and 1170 K. The different thermal expansion behavior is already evident from inspection of Fig. 1. The largest principal axis of the thermal expansion is given by α_1 with a marked nonlinear variation toward the phase transition temperature; α_3 is intermediate, but decreases distinctly from 12.6 to 10.5 $\times$ 10^{-6} K^{-1} at the phase transition. As the principal axes α_1 and α_3 are allowed to rotate within the **a**–**c** plane in the monoclinic system, the orientation of α_3 to the **c**-axis was also calculated and its variation with temperature is displayed in Fig. 2c. It is evident that not only the magnitude but also the orientation of the thermal expansion ellipsoid is rearranged as a function of temperature. While the angle between the **c**-axis and α_3 is ~30° (toward the positive *a*-axis) at low temperatures, α_3 is continuously rotated toward the **c**-axis to arrive at an angle of −13.5° at around 1130 K, shortly before the phase transition occurs. At the phase transition, a rotation by ~20° away from **c**-axis takes place (Table 4). Concluding, the largest thermal expansion in $LiCrGe_2O_6$ in the $P2_1/c$ phase is within the **a**–**c** plane, with the largest thermal expansibility between the sheets of M sites (see Fig. 3), intermediate values with variable angles in chain direction of M1 and T sites, and smallest values parallel to the **b**-axis. In $C2/c$, the thermal expansion is dominated by the **b**-axis, as is common in all $C2/c$ pyroxenes (Tribaudino and Mantovani 2014); here, the symmetrically equivalent tetrahedral chains obviously are more stiff as compared to the $P2_1/c$ phase and show only minor thermal expansion, determining the low expansibility along *c*. $LiFeGe_2O_6$ shows similar thermal expansion of the lattice (Redhammer et al. 2010b).

Table 3 Selected bond lengths (Å) and angles at some representative temperatures for synthetic $LiCrGe_2O_6$ pyroxene as extracted from Rietveld refinements of neutron diffraction data

Temp (K)	3	10	310	1073	1173	1273
S.G.	$P2_1/c$	$P2_1/c$	$P2_1/c$	$P2_1/c$	$C2/c$	$C2/c$
Cr–O1A^{v} (Å)	2.056(3)	2.060(3)	2.049(3)	2.065(3)	2.062(4)	2.071(4)
Cr–O1B (Å)	2.063(3)	2.064(3)	2.055(4)	2.072(3)	–	–
Cr–O1A^{vi} (Å)	1.995(3)	1.996(3)	1.986(3)	2.011(3)	2.034(2)	2.037(2)
Cr–O1B^{ii} (Å)	2.021(3)	2.021(3)	2.033(3)	2.040(3)	–	–
Cr–O2A^{v} (Å)	1.889(3)	1.888(3)	1.907(3)	1.921(3)	1.921(4)	1.931(4)
Cr–O2B^{vii} (Å)	1.950(3)	1.944(3)	1.941(3)	1.953(3)	–	–
<Co1–O> (Å)	1.996	1.996	1.995	2.010	2.006	2.013
Cr1–Cr1$_{(intra)}$ (Å)	3.110(2)	3.114(2)	3.104(2)	3.128(2)	3.147(2)	3.150(2)
Cr1–Cr1$_{(GeA)}$ (Å)	5.449(2)	5.452(2)	5.469(2)	5.535(2)	5.594(2)	5.616(2)
Cr1–Cr1$_{(GeB)}$ (Å)	5.574(2)	5.563(2)	5.591(2)	5.621(2)	–	–
Cr–O1A^{v}–Cr^{ii} (°)	100.3(2)	100.3(2)	100.6(2)	100.1(2)	100.4(2)	100.1(2)
Cr–O1B^{ii}–Cr^{ii} (°)	99.2(2)	99.3(2)	98.8(2)	99.0(2)		
Li–O1A^{i} (Å)	2.114(6)	2.111(6)	2.125(7)	2.211(9)	2.217(9)	2.195(9)
Li–O1B^{ii} (Å)	2.108(6)	2.103(6)	2.122(7)	2.155(8)	–	–
Li–O2A^{v} (Å)	2.328(6)	2.329(5)	2.340(6)	2.444(9)	2.441(8)	2.440(9)
Li–O2B^{iv} (Å)	2.011(6)	2.008(6)	2.036(6)	2.088(9)	–	–
Li–O3A (Å)	2.143(6)	2.147(5)	2.154(6)	2.201(9)	2.217(9)	2.343(9)
Li–O3B^{iii} (Å)	3.232(6)	2.346(6)	2.372(8)	2.527(9)	–	–
<Li–O> (Å)	2.174	2.174	2.191	2.271	2.314	2.326
GeA–O1A (Å)	1.765(2)	1.767(2)	1.767(2)	1.757(2)	1.757(3)	1.762(2)
GeA–O2A (Å)	1.714(2)	1.716(2)	1.706(2)	1.692(3)	1.695(3)	1.693(3)
GeA–O3A (Å)	1.751(2)	1.750(2)	1.744(2)	1.748(2)	1.736(3)	1.731(3)
GeA–O3A (Å)	1.752(2)	1.752(2)	1.753(2)	1.752(2)	1.756(3)	1.758(3)
<GeA–O> (Å)	1.746	1.746	1.742	1.737(2)	1.736	1.736
τ (°) GeA	111.6(1)	111.5(1)	111.4(1)	110.7(1)	111.9(1)	112.1(1)
GeA–O3A–GeA (°)	127.1(1)	127.3(1)	127.9(1)	129.9(1)	134.5(1)	134.9(1)
O3A–O3A–O3A (°)	210.4(1)	210.5(1)	209.6(1)	205.9(1)	190.2(1)	189.8(1)
GeB–O1B (Å)	1.764(2)	1.765(2)	1.758(2)	1.737(2)	–	–
GeB–O2B (Å)	1.708(2)	1.710(2)	1.706(2)	1.714(2)	–	–
GeB–O3B (Å)	1.766(2)	1.765(2)	1.763(2)	1.759(2)	–	–
GeB–O3B (Å)	1.768(2)	1.766(2)	1.772(2)	1.761(2)	–	–
<Ge–O>$_B$ (Å)	1.751	1.751	1.750	1.743	–	–
τ (°) GeB (°)	110.2(1)	110.2(2)	110.4(1)	110.8(1)		
GeB–O3B–GeB (°)	123.7(1)	123.6(1)	124.0(1)	129.5(1)	–	–
O3B–O3B–O3B (°)	135.9(1)	135.9(1)	136.6(1)	146.1(1)	–	–

For symmetry codes, see Fig. 3. τ (°) = average of O–Ge–O angles involving the O1 apex oxygen atom of the tetrahedron (see text)

Structural evolution with temperature

Between 0.5 and 1140 K, the pyroxene compound $LiCrGe_2O_6$ shows the $P2_1/c$ symmetry. Here, the crystal structure is characterized by one symmetry-independent Li site (M2), one independent Cr^{3+} (M1) site, and two independent tetrahedral sites, GeA and GeB, giving rise to two independent tetrahedral chains, which have different kinking states and also different bond lengths and distortional parameters. As is typical for the $P2_1/c$ pyroxenes, the GeA chain is S (same)-rotated, thus showing a kinking angle O3A^{x}–O3A–O3A^{xi} > 180°, while the GeB chain is O (opposite)-rotated, with the O3B–O3B^{iii}–O3B^{iv} angle being <180° (Redhammer and Roth 2004a). Both in the M1 as well as in the M2 polyhedron, there are six different bonds from the cations to the surrounding oxygen atoms. Above 1140 K, the neutron powder diffraction data can be indexed and refined with $C2/c$ space group. Here, only one distinct tetrahedral chain

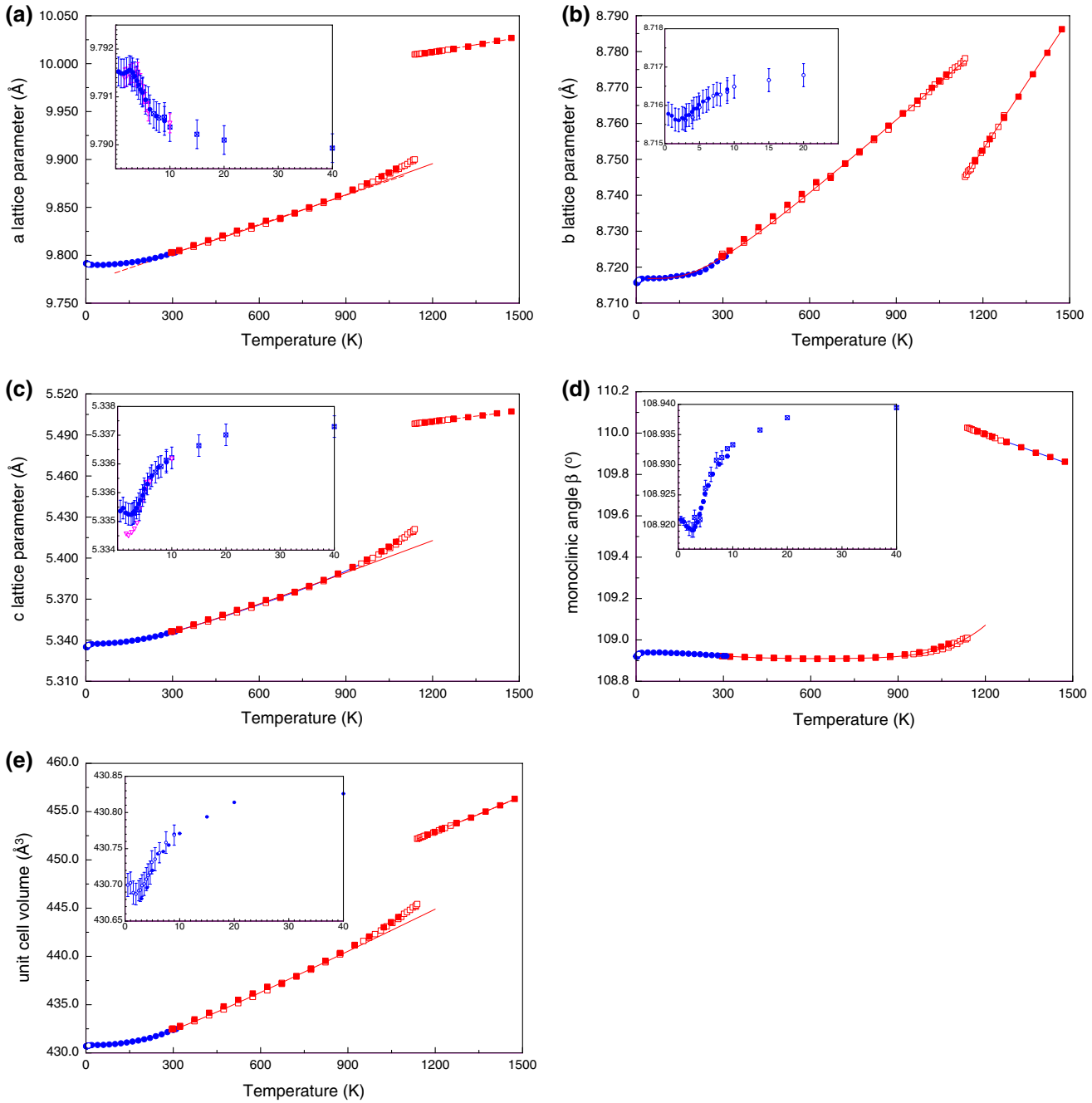

Fig. 1 Evolution of lattice parameters of $LiCrGe_2O_6$ with temperature. The *insets* show the low-temperature data on an enlarged scale, with *filled squares* representing the $\lambda = 1.5482$ Å measurements, *open triangles* the $\lambda = 2.436$ Å measurements at SPODI

with S-rotational sense is present; the kinking angle of this chain is between 191° and 189°; thus, $LiCrGe_2O_6$ shows the so-called high-temperature form of the two possible *C*2/*c* modifications. Diagrams of the crystal structure in the $P2_1/c$ (298 K) and *C*2/*c* (1173 K) modification are shown in Fig. 3, to facilitate crystal chemical discussion given below. Generally, the variations in structural parameters are smooth and consistent within one experimental setup; however, some changes in slope and different absolute values in thermal parameters, bond lengths, and angles for similar temperatures are evident between the low-temperature cryostat and high-temperature furnace setup.

Atomic displacement parameters

Between base temperature (4 K) and 200 K, the atomic displacement parameters (ADPs) were refined in their isotropic form, while between 200 and 473 K, the

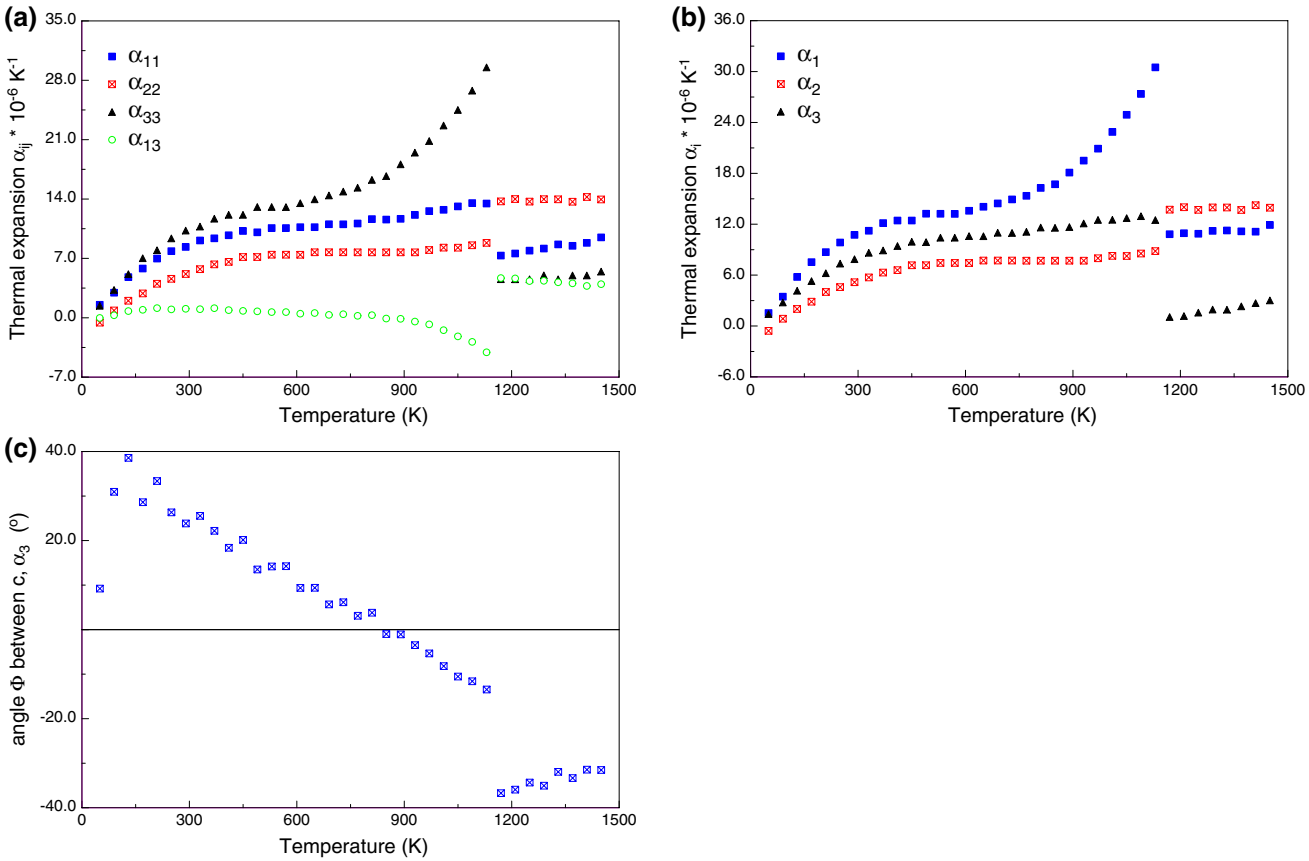

Fig. 2 Axial thermal expansion coefficients α_{ij} (**a**), main axis α_i of the thermal ellipsoid (**b**), and angle Φ defining the orientation of α_3 with respect to the crystallographic *c*-axis (**c**)

Table 4 Axial thermal expansion coefficients and principal axis lengths of the thermal expansion ellipsoid calculated for different temperature intervals in $LiCrGe_2O_6$

	Axial thermal expansion element $\times 10^{-6}$ K^{-1}				Main ellipsoid axes $\times 10^{-6}$ K^{-1}			Angle α_3, **c**
T (K)	$\alpha_{(11)}$	$\alpha_{(22)}$	$\alpha_{(33)}$	$\alpha_{(13)}$	α_1	α_2	α_3	Φ (°)
230–270	7.850	4.590	9.360	0.99	9.85	4.59	7.36	26.33
310–350	9.120	5.730	10.75	1.01	11.23	5.73	8.637	25.55
430–470	10.23	7.160	12.14	0.81	12.44	7.16	9.933	20.15
630–670	10.68	7.720	13.97	0.56	14.06	7.72	10.59	9.40
830–870	11.58	7.710	16.71	−0.009	16.71	7.71	11.58	−1.00
1030–1070	13.13	8.260	24.50	−2.19	24.91	8.26	12.72	−10.53
1110–1150	13.47	8.830	29.52	−4.07	30.49	8.83	12.5	−13.45
C2/c								
1150–1190	7.330	13.72	4.550	4.68	10.82	13.72	1.58	−36.73
1230–1270	7.920	13.70	4.540	4.33	10.88	13.78	1.82	−34.34
1430–1470	9.480	13.95	5.450	3.96	11.91	13.95	3.22	−31.52

displacement of the Li atom, and above 473 K, the displacement of all atoms was treated in the anisotropic form. At low temperatures, the largest equivalent isotropic ADP is observed for the Li atom, levelling off to a value of ~0.5 even at base temperature (Fig. 4). Similar large values are also found for the O2B, O3A, and the O2A oxygen atoms, approaching values of ~0.4, 0.25, and 0.20, respectively, toward $T = 0$ K. The Cr, GeA, and GeB atoms have the smallest ADPs, being close to zero at $T = 0$ K, as it is expected for atoms without positional disorder and in the absence of anharmonic contributions to the ADP (Willis and Pyror 1975; Prencipe et al. 2000). The positive

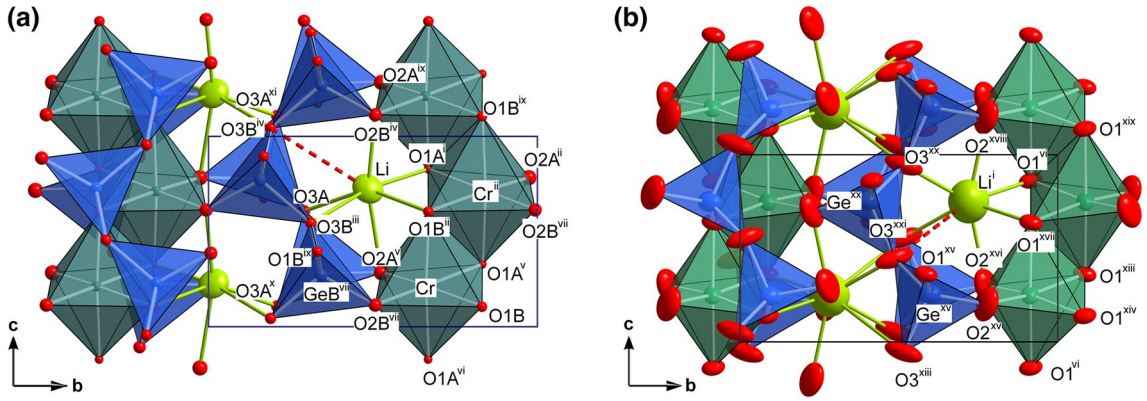

Fig. 3 Polyhedral drawings of the structure of $LiCrGe_2O_6$ at 298 K in the $P2_1/c$ (**a**) and at 1173 K in the $C2/c$ phase (**b**). The nomenclature for selected atoms is given; thermal ellipsoid plotted at 75 % probability level, symmetry codes: (i) $-x$, $1-y$, $1-z$; (ii) x, $1.5-y$, $0.5+z$; (iii) $1-x$, $1-y$, $1-z$; (iv) $1-x$. $1-y$, $1.5-z$; (v) $-x$, $0.5+y$, $0.5-z$; (vi) $-x$, $1-y$, $-z$; (vii) $1-x$, $-0.5+y$, $0.5-z$; (viii) $1-x$, $2-y$, $1-z$; (ix) x, y, $1+z$; (x) x, $0.5-y$, $-0.5+z$; (xi) x, $0.5-y$, $0.5+z$; (xii) $1-x$, $1-y$, $1-z$; (xiii) $-x$, $1+y$, $0.5-z$; (xiv) x, $1+y$, z; (xv) $0.5-x$, $0.5+y$, $0.5-z$; (xvi) $-0.5+x$, $0.5+y$, z; (xvii) x, $1-y$, $0.5+z$; (xviii) $0.5-x$, $0.5+y$, $1.5-z$; (xix) x, $1+y$, $1+z$; (xx) $0.5-x$, $0.5-y$, $1-z$; (xxi) $-0.5+x$, $0.5-y$, $0.5+z$; (xxii) $0.5-x$, $0.5+y$, $-z$

intercepts of ADPs at $T = 0$ K may therefore be seen as an indication of small positional disorder, however, can also be the effect of quantum mechanical zero-point fluctuations. Toward high temperatures, the ADP of Li distinctly increases nonlinearly above 800 K and remains the largest one among all atoms. As at higher temperature linear harmonic contributions prevail the size of the ADPs, this nonlinear behavior can be seen as an indication of increasing positional disorder as the phase transition temperature is approached. Large thermal motions are also observed for the O2 and O3 oxygen atoms; the increase with T—however—is almost linear above room temperature. The large values for these atoms indicate that there is a significant structural instability/flexibility with respect to the interconnection of individual GeO_4 tetrahedra via the O3 oxygen atoms and the lateral connection of the tetrahedral chains with the octahedral chain via the O2 oxygen atoms. O3 and O2 oxygen atoms form the basal plane of the tetrahedron (Fig. 3), and all oxygen atoms are affected by a change in the kinking state (O3–O3–O3 angle) of the tetrahedral chain. Small and similar in size are the ADPs for the Ge, the Cr and the O1 oxygen atoms, and their increase scales linearly with temperature. The O1A and O1B oxygen atoms are the apex oxygen atoms of the tetrahedron and connect the tetrahedral and octahedral chains along the **a**-axis. The structural phase transition was marked by an increase in equivalent isotropic atomic displacement parameters, especially for the O2 and O3 atoms (Fig. 4) and for the Li atom, whereas the ones of O1, Ge, and Cr atoms remain similar in the $P2_1/c$ and $C2/c$ phases. Thus, in the latter three distinct groups of ADPs can be identified (Fig. 4) with the O2 and O3 oxygen atoms being intermediate between Li and O1, Cr, and Ge atoms. The temperature variation here is linear.

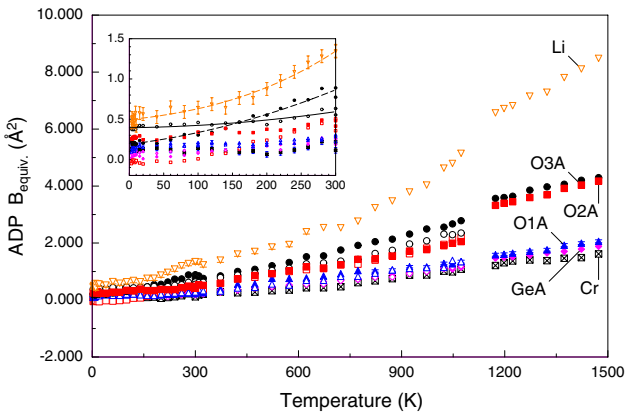

Fig. 4 Variation in equivalent isotropic atomic displacement parameters B_{eq} with temperature for $LiCrGe_2O_6$; *inset* zoomed in temperature range between 0.5 and 300 K

The M2 site

The M2 site in $LiCrGe_2O_6$ is sixfold coordinated with Li–O bonds, ranging from 2.021(6) to 2.343(6) Å at room temperature; the coordination polyhedron can be described as a strongly distorted octahedron. Four Li–O bonds connect the M2 with the M1 octahedra, while the two Li–O3A and Li–O3B^{iii} bonds link it to the tetrahedral chains (see Fig. 3a for a polyhedral drawing and definition of symmetry codes). Average Li–O bonds remain constant at ~2.174(5) Å up to temperatures of ~150 K, while they increase linearly by 0.096 Å to 2.271(5) Å at 1073 K (Fig. 5a). This gives rise to an average thermal expansion of the Li–O

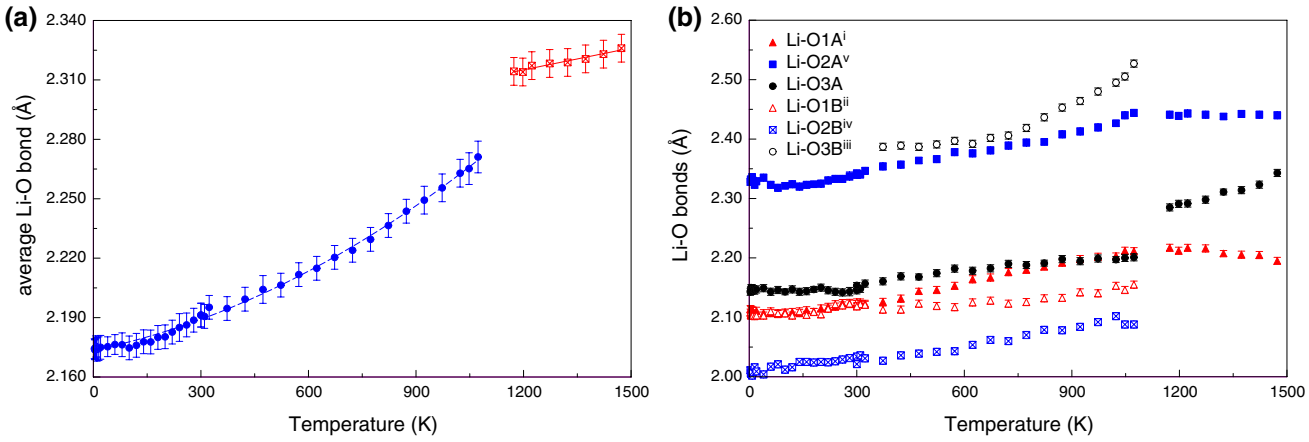

Fig. 5 Variation in average (**a**) and individual (**b**) Li–O bond lengths in $LiCrGe_2O_6$ as a function of temperature

bond $\alpha_{<Li-O>} = 47.7 \times 10^{-6}$ K^{-1} with $\alpha = (l_T - l_0)/[l_0*(T - T_0)]$, where l_T is the length at temperature T (1073 K) and l_0 is the length at $T_0 = 200$ K. In the pyroxene-type compound $LiFeGe_2O_6$, a similar bond length expansion of 38.9×10^{-6} K^{-1} was observed (Redhammer et al. 2010b). At the $P2_1/c$–$C2/c$ phase transition, <Li–O> increases by ~0.043 Å to 2.314(6) Å (at 1173 K); within the $C2/c$ phase, <Li–O> bonds increase linearly, but with smaller slope and an average linear thermal expansion of $\alpha_{<Li-O>} = 16.8 \times 10^{-6}$ K^{-1}.

The individual Li–O bonds show different temperature variations, with the smallest increase found for Li–O1B^{ii}; similarly, small changes are observed for the Li–O2B^{iv} and the Li–O3A bonds. The Li–O1A^{i} and Li–O2A^{v} bond lengths change on the average by 0.10 and 0.12 Å between 200 and 1073 K, while the largest increase takes place for the Li–O3B^{iii} bond lengths, which increase by as much as 0.17 Å with some distinct nonlinear increase toward the phase transition temperature. The bond length distortion increases also gradually within the $P2_1/c$ phase. At the phase transition, the Li bonds to the A and B oxygen atoms become equivalent; changes in <Li–O> are mainly controlled by the Li–O2 and Li–O3 bonds, as was observed for $LiFeGe_2O_6$ also (Redhammer et al. 2010b). Especially for the Li–O2B^{iv}, this is associated with large alterations in the bond lengths by +0.35 Å when becoming equivalent with the A oxygen atoms to form the Li–O2 bonds in the $C2/c$ phase. For the Li–O3 bonds, distinct jumps in the bonding topology occur: The Li–O3A bond is stretched from 2.148(6) in $P2_1/c$ to 2.286(6) Å in $C2/c$. The Li–O3B^{iii} bond, however, is extended from 2.372(6) to 3.234(6) Å and no longer belongs to the coordination polyhedron around Li^+. Vice versa, the Li–O3B^{iv} contact is reduced from 3.126(6) Å to 2.286(6) Å and thus becomes bonding. These distinct movements of the O3 oxygen atoms by as much as 0.84 Å are the direct consequence of the altered kinking state of the tetrahedral chains in the $C2/c$ phase. Within the $C2/c$ phase, only the Li–O3 bond length increases with increasing temperature; the thermal expansion of this distance is three times larger than the one of the Li–O3A and still larger than the one of the Li–O3B^{iii} bond in the $P2_1/c$ phase. On the contrary, the Li–O1 bond shows a negative thermal expansion and Li–O2 bond length stays constant. This is further evidence for the different thermal expansion of the lattice in $P2_1/c$ and $C2/c$. The larger thermal expansions of Li–O3 bonds, which point in **b** direction, contribute to the larger thermal expansion of the **b**-axis in $C2/c$ as compared to $P2_1/c$.

The M1 site

Similar to <Li–O>, the average Cr–O bond increases with T, however, to a much smaller extent as is expressed by the average linear thermal expansion coefficient $\alpha_{<Cr-O>} = 8.7 \times 10^{-6}$ K^{-1} for the T interval of 200–1140 K. This bond length expansion is slightly smaller than the one found for the M1 site in $LiFeGe_2O_6$ with $\alpha_{<Fe-O>} = 10.8 \times 10^{-6}$ K^{-1} (Redhammer et al. 2010a, b). Up to room temperature, <Cr–O> bond remains almost constant. At the phase transition, <Cr–O> becomes shortened by ~0.05 Å; in the $C2/c$ phase, the thermal expansion is larger with $\alpha_{<Cr-O>} = 12.0 \times 10^{-5}$ K^{-1} (Fig. 6a).

Individual Cr–O bonds show different temperature variations: The Cr–O2A^{v} bond lengths increase with T from base temperature to room temperature, while the Cr–O2B^{vii} bond decreases at a similar rate, i.e., the two bonds become more equal; above ~300 K, they both increase with T (Fig. 6b) at the same extent with a thermal expansion $\alpha = 8.9$ and 8.0×10^{-6} K^{-1}, respectively. The Cr–O2 bond in the $C2/c$ phase is similar to the value of the Cr–O2A^{v} bond; the Cr–O2B^{vii} bond is shorted at the phase transition by 1.6 %. A similar behavior is observed for the Cr–O1A^{vi}

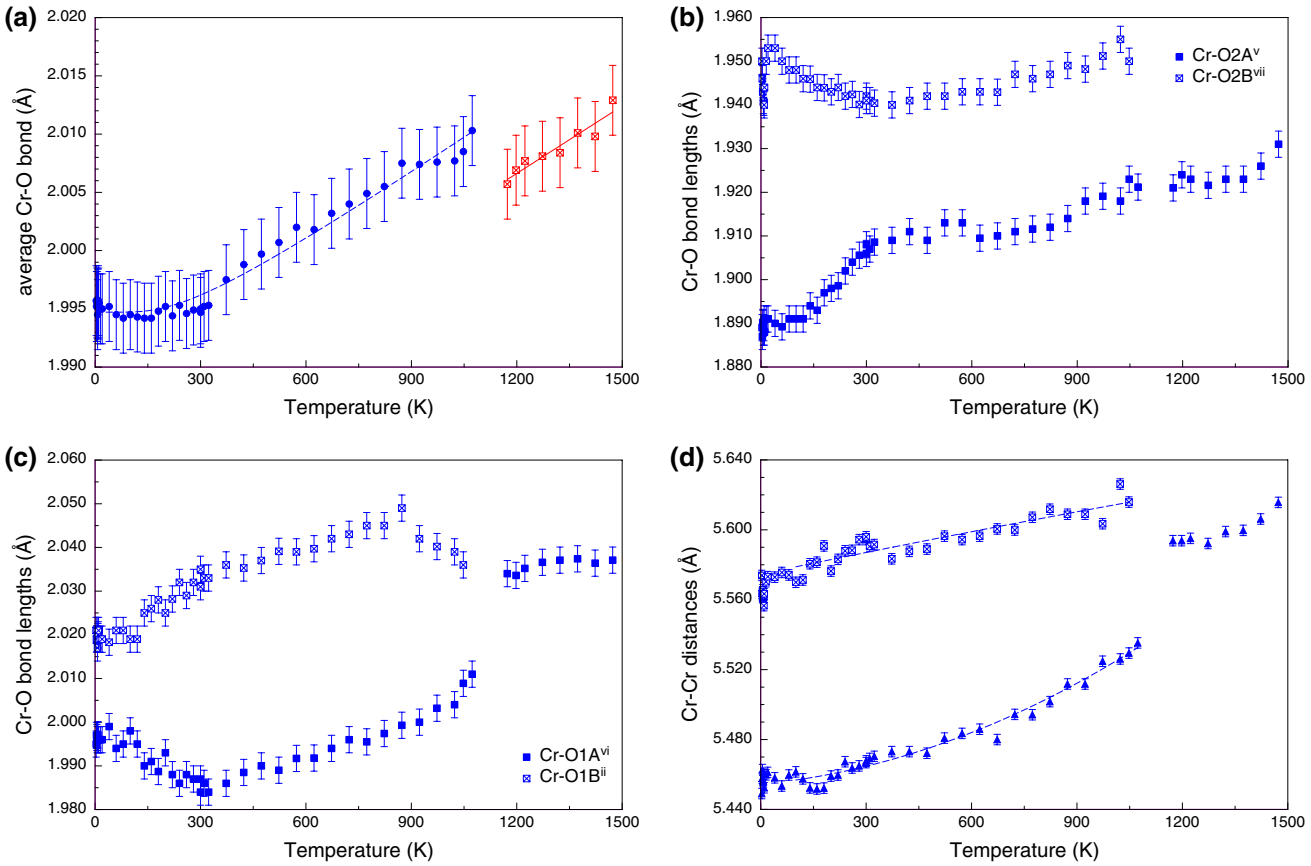

Fig. 6 Evolution of bond lengths and inter-atomic distances for the M1 site in $LiCrGe_2O_6$ with temperature **a** average Cr–O bond length, **b**, **c** individual Cr–O bond lengths, **d** shortest Cr–Cr distances between neighboring M1 chains

and Cr–O1B^{ii} bonds, which run parallel to the *c*-axis to the apex oxygen atoms of the octahedra. Here also, one of the two bonds (Cr–O1B), which become equivalent at the phase transition, increases with *T* from 10 K to ~300 K, while the second (Cr–O1A) decreases; thus, the two bonds become less equal toward 298 K. Above room temperature, both bonds increase with the Cr–O1A bond having a larger thermal expansion of 17.6×10^{-6} K^{-1}; above 900 K, the Cr–O1B bond tends to decrease again, approaching the bond length value found in the *C*2/*c* modification (Fig. 6c) and decreasing the difference between the two Cr–O1A, Cr–O1B bonds already within the $P2_1/c$ phase. At the phase transition, the Cr–O1A bond increases by 1.1 %. The relative changes in the Cr–O2B and Cr–O1A bonds at the phase transition have the same sign, but smaller numeric values than those of the equivalent bonds in $LiFeGe_2O_6$, changing by 2.4 and 1.6 %, respectively (Redhammer et al. 2010b). Generally, the changes in structural parameters at the $P2_1/c$ to *C*2/*c* phase transition are less pronounced in $LiCrGe_2O_6$ than the ones in the iron compound.

In the *C*2/*c* phase, all individual Cr–O bonds increase with temperature in a linear manner; the largest expansion is found for the Cr–O2 bond ($\alpha = 17.4 \times 10^{-6}$ K^{-1}), the smallest one for the Cr–O1 bonds to the apex oxygen atoms ($\alpha = 5.1 \times 10^{-6}$ K^{-1}). This corresponds to a reversal of the ranking of the thermal expansion with respect to the $P2_1/c$ phase. In *C*2/*c*, the octahedra expand less along the **c**-axis, while the expansion along **b**, mediated by the Cr–O2 bonds, is enhanced.

Above 200 K, the Cr–Cr^{ii} distances within the M1 chain increase almost linearly with temperature up to 3.128 (2) Å at 1073 K, with an average linear thermal expansion coefficient of 6.9×10^{-6} K^{-1}. At the phase transition, the Cr atoms move further away from each other by ~0.02 Å, resulting in a distance of 3.147(2) Å at 1173 K. Within the *C*2/*c* phase, the expansion of Cr–Cr along *c* is smaller (3.6×10^{-6} K^{-1}), meeting the general trend seen also in the Cr–O distances. The two different Cr–Cr distances between the M1 chains show a larger expansion; especially, the shorter one, which involves the GeA tetrahedron, increases distinctly between 200 and 1073 K (Fig. 6d) with an average linear thermal expansion of 16.0×10^{-6} K^{-1}, as compared to the one, involving the GeB tetrahedral chain, with 9.2×10^{-6} K^{-1}. The thermal expansion between the M1 chains is largely controlled by the kinking state of the tetrahedral chains and by the expansion of Li–O3 bonds.

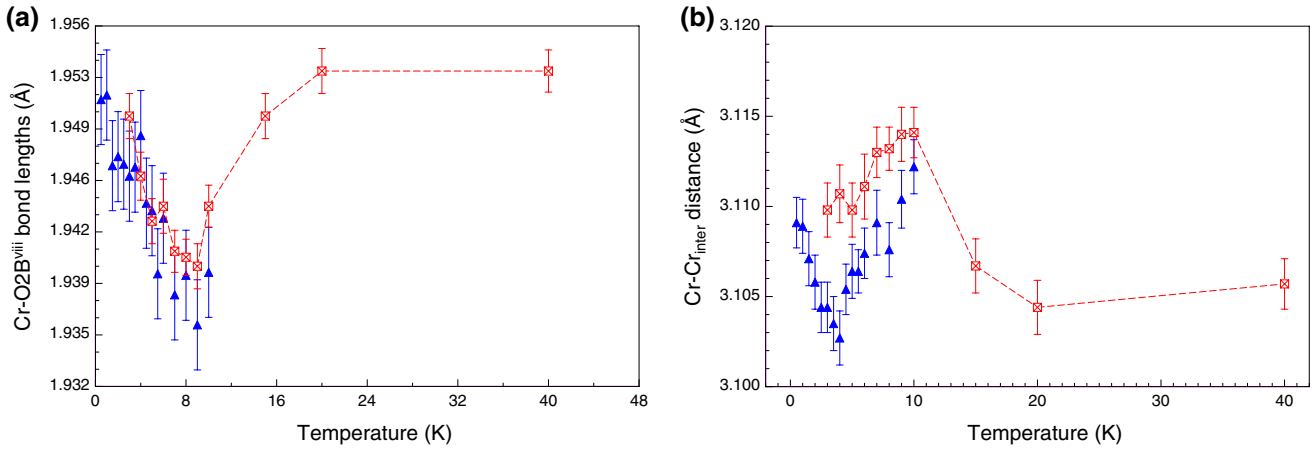

Fig. 7 Evolution of bond lengths and inter-atomic distances for the M1 site in $LiCrGe_2O_6$ in the low-temperature region **a** individual Cr–O2B^{vii} bond lengths, **b** shortest Cr–Cr^{ii} distances within the M1 chains; the two different curves correspond to the two different wavelengths used in the experiments

A detailed inspection of the low-temperature region (T < 40 K) of the $P2_1/c$ phase reveals some additional changes in the Cr–O bonds, which are associated with the magnetic phase transition. This applies for the Cr–O1A^{v} bond in the equatorial plane of the octahedron, which decreases slightly in the magnetically ordered phase, while the Cr–O2B^{vii} bond length increases on the contrary (Fig. 7a). The data sets with the two different wavelengths ($\lambda = 1.5482$ Å and $\lambda = 2.436$ Å) in the low-temperature region plot well onto each other and show very similar trends. No significant changes are observed in the 0.5–15 K region for the other four Cr–O bonds. This is indicative of a successive change in the Cr–O bonds along the O1A^{v}–O2B^{vii} diagonal axis within the equatorial plane of the octahedron with a movement of the Cr atom. This is deduced from the nonlinear variation in the shortest Cr–Cr^{ii} distance within the M1 chain. This increases slightly below 25 K toward 10 K, decreases between 10 and ~5 K, and increases again toward very low temperatures. This trend is evident in both measurement series and is directly related to the magnetoelastic coupling between Cr–Cr^{ii} atoms (Fig. 7b). Among the two different Cr–Cr distances between the M1 chains, the shorter one, involving the GeA chain, remains constant when passing the magnetic phase transition temperature, while the larger one, involving the GeB chain, increases significantly below 5 K. From this, it can be concluded that in the magnetic pre-ordering region below 10 K, the intra- as well as the inter-chain Cr–Cr distances become somewhat shorter, but with the full development of antiferromagnetic magnetic ordering below 6 K; the Cr–Cr distances again become larger. The data for the Cr–O1A^{v} and O1B^{ii}–Cr^{ii} bond angles scatter too much to deduce a clear picture.

The Ge sites

The Ge tetrahedra behave as rigid units with only small changes in bond lengths as a function of temperature. Remarkably, a small negative thermal expansion of -3.7×10^{-6} K^{-1} for <GeA–O> and -5.7×10^{-6} K^{-1} for the <GeB–O> bond length (Fig. 8a; Table 3) is found in the $P2_1/c$ phase. $LiFeGe_2O_6$ shows very similar average Ge–O bond lengths, and for this compound, a decrease in average and individual Ge–O bond lengths with increasing T was also reported by Redhammer et al. (2010b), further supporting that this effect is significant although quite small. In $LiCrGe_2O_6$, there is no significant discontinuity in <Ge–O> bond lengths at the phase transition. In the $C2/c$ phase, <Ge–O> bond remains constant with T. Among the individual bond lengths, the smallest is the one to the O2(A,B) oxygen atom, both in the A— as well as in the B chain, while bonds to the apex oxygen O1(A,B) and the ones to the O3 bridging atoms are of similar lengths; all individual bonds decrease with T in the $P2_1/c$ phase to the same extent as is observed for the average Ge–O bonds. Apart from these small changes in bond lengths, there are some more pronounced alterations found in bond angles. This is most prominent for the GeA–O3A–GeA and GeB^{vii}–O3B^{iii}–GeB^{xii} angles which increase successively with increasing T by 2.7° and 5.8° between 200 and 1073 K (Fig. 8b). Close to the phase transition temperature, both angles approach each other. Increasing the Ge–O–Ge angle causes a stretching of the tetrahedral chain along the **c**-axis. This is how the structure manages to the match the very different thermal expansion of octahedral and tetrahedral chains. The angle τ, which is the average of the three O–Ge–O bond angles, involving the O1 apex oxygen atom of the tetrahedron, increases

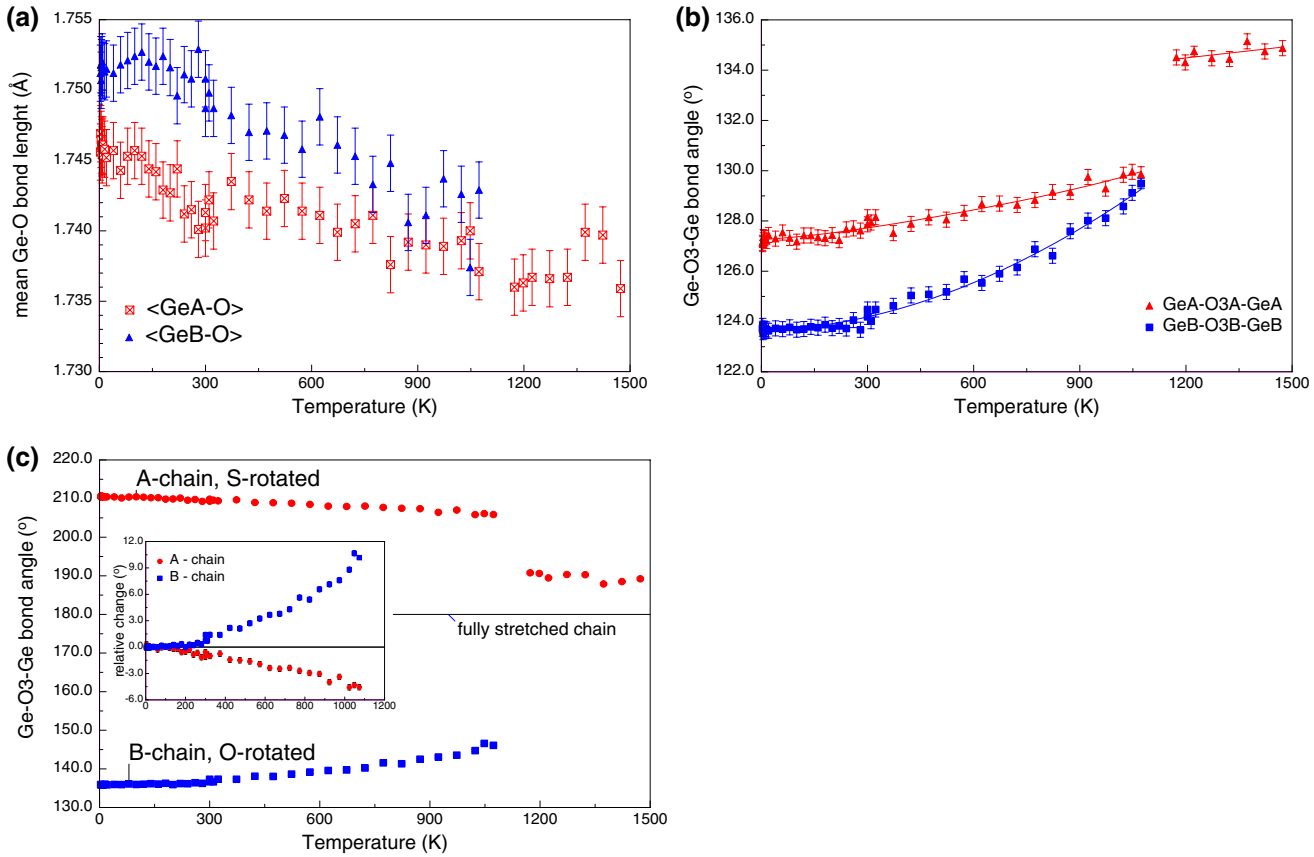

Fig. 8 Evolution of structural parameters for the tetrahedral sites in LiCrGe2O6 with temperature: **a** average bond lengths, **b** Ge–O–Ge bond angle, and **c** tetrahedral O3–O3–O3 kinking angle; the *inset* in **c** shows the relative change of the kinking angle in the $P2_1/c$ phase with respect to the 3 K data

slightly at both sites, indicating an increasing elongation of the tetrahedra along the **a** direction with increasing temperature. In the *C*2/*c* phase, the tetrahedra are more elongated along the **c**-axis (larger Ge–O3–Ge angles), but also more elongated along the **a**-axis as expressed by a larger angle τ. These observations meet perfectly the ones also found for $LiFeGe_2O_6$.

Both tetrahedral chains expand as a whole with increasing temperature by increasing (chain B) or decreasing (chain A) the tetrahedral kinking angle. The observed variation with temperature in the $P2_1/c$ phase is ~5° for the A chain and twice more than that for the B chain, which, however, is generally the more kinked chain. At the phase transition, close to the point where the two chains become equivalent, the kinking angle of the B chain changes by ~45° and switches from O-rotated to S-rotated; the A chain remains S-rotated and extends by ~15° at the transition. The strong deformation of the M2 site at the phase transition is a direct consequence of these alterations in tetrahedral chain geometry. In the *C*2/*c* phase, the kinking angle still decreases with increasing temperature, extending the chain. It should be noted that among the known *C*2/*c* pyroxenes S-rotated chains are rare, most of them belong to the series of Li pyroxenes, and all of them have almost fully extended tetrahedral chains.

The magnetic phase transition

First, additional Bragg reflections in the neutron diffraction data, indicative of magnetic ordering, appear between 7 and 6 K (Fig. 9). This is somewhat higher than reported in the literature so far (~3 K).

The magnetic reflections can be indexed in space group $P2_1/c$ with a propagation vector of $\boldsymbol{k} = (0, 0, 0)$. The possible magnetic structures, compatible with this $P2_1/c$ symmetry of $LiCrGe_2O_6$, were determined by representational analysis and calculated with BasiReps (Rodríguez-Carvajal 2001) using the projection operation technique. Results are summarized in Tables 5 and 6. Refinement of these possible magnetic structures against the 0.5 K data showed that among the four possible irreducible representations, only one gives satisfactory description of the magnetic structure of $LiCrGe_2O_6$, which is Γ_4 of Table 6 with the basis functions [C_x, A_y, C_z] and $R_{mag} = 5.47$ %; the resulting

magnetic space group is $P2_1'/c$. This model of the magnetic structure has a pure antiferromagnetic arrangement of spins, both within and between the M1 chains. There is no difference in inter-chain coupling, independently, whether the M1 chains are coupled via the GeA or the GeB tetrahedral chains. A diagram of the magnetic structure is displayed in Fig. 10. The determined spin structure of this study is in excellent agreement with the data at 1.7 K of Nenert et al. (2010b), including the size of the magnetic moment $\mu(Cr^{3+}) = 2.33(3)$ μB and orientation of spins (30.3(1)° with respect to the **a**-axis); the corresponding values of this study at 2 K are $\mu(Cr^{3+}) = 2.34(6)$ μB and 29.8(2)°, respectively. However, the statement of ferromagnetically coupled M1 chains in Nenert et al. (2010b) is misleading as the Cr^{3+} atoms, which would have a ferromagnetic coupling, are 6.459(4) Å away from each other at 3 K, while the closer Cr–Cr distances are 5.449(3) Å and 5.574(3) Å via GeA and GeB tetrahedral sites, respectively. The latter distances are assumed to take part in magnetic super-superexchange only (Table 7).

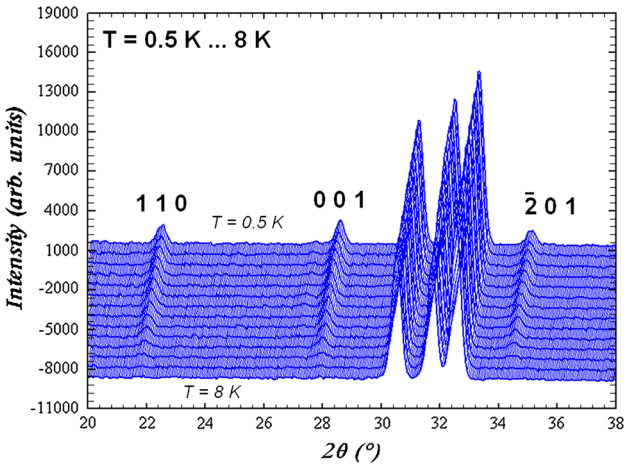

Fig. 9 Part of the neutron diffraction pattern of $LiCrGe_2O_6$, displaying the appearance of magnetic Bragg peaks at low temperatures; the *T* increment is 0.5 K, starting at 0.5 K

The appearance of AFM coupling within the M1 chains in $LiCrGe_2O_6$ is consistent with large Cr–O–Cr angles of 100.3(1)° and 99.2(1)° for both possible intra-chain exchange pathways Cr–O1A–Cr and Cr–O1B–Cr, respectively, in the germanate. Following the Goodenough–Kanamori rules (Goodenough 1963), only values close to a rectangular M–O–M geometry would favor ferromagnetic

Table 5 Cr positions at the 4e site in $LiCrGe_2O_6$ in space group $P2_1/c$ within one primitive unit cell at 3 K

Label (G_k)	Elem.	Symm. op.	+ (*x*, *y*, *z*)	*x*	*y*	*z*
Cr_1	1	*x*, *y*, *z*	0, 0, 0	0.2509	0.6583	0.2140
Cr_2	2	$-x, y+0.5, -z+0.5$	1, −1, 0	0.7509	0.1583	0.2860
Cr_3	−1	$-x, -y, -z$	1, 1, 1	0.7509	0.3417	0.7860
Cr_4	c	$x, -y+0.5, z+0.5$	0, 1, 0	0.2509	0.8417	0.7740

Table 6 Possible magnetic structures based on basis vector analysis for $LiCrGe_2O_6$ in space group $P2_1/c$ and resulting magnetic space groups according to Litvin (2008)

	Cr_1	Cr_2	Cr_3	Cr_4	Basis funct.	Magn. S.G.
Γ_1	[u v w]	[−u v −w]	[−u −u −w]	[u −v w]	$A_x C_y A_z$	$P2_1/c'$
Γ_2	[u v w]	[−u v −w]	[u v w]	[−u v −w]	$G_x F_y G_z$	$P2_1/c$
Γ_3	[u v w]	[u −v w]	[u v w]	[u −v w]	$F_x G_y F_z$	$P2_1'/c'$
Γ_4	[u v w]	[u −v w]	[−u −v −w]	[−u v −w]	$C_x A_y C_z$	$P2_1'/c$

A = +−−+; C = ++−−; G = +−+−; F = ++++ following the notation of Bertaut (1968)

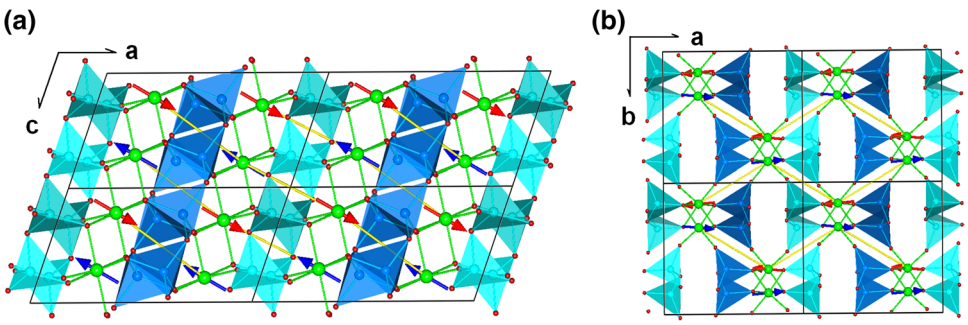

Fig. 10 Diagrams of the magnetic structure of $LiCrGe_2O_6$ at 0.5 K (*left along* **b**, *right along* **c*** direction)

Table 7 Components along **a**- and **c**-axes and resulting total magnetic moments in synthetic $LiCrGe_2O_6$ as extracted from Rietveld refinements of neutron diffraction data

	0.5 K	1.0 K	2.0 K	4.0 K
M_x (M1) (μ_B)	2.25(8)	2.18(5)	2.43(7)	2.17(7)
M_z (M1) (μ_B)	1.17(13)	1.10(8)	1.23(11)	1.06(12)
M_{M1} (μ_B)	2.18	2.10	2.34	2.08
$\angle$(**a**, M_{M1}) (°)	30.5(2)	39.6(2)	29.8(2)	28.7(29
J_1 in chain	AFM	AFM	AFM	AFM
J_2 between chains	AFM	AFM	AFM	AFM
Magn. space group	$P2_1'/c$	$P2_1'/c$	$P2_1'/c$	$P2_1'/c$

$\angle$(**a**, M_{M1}) = angle between the magnetic moment at the M1 site and the crystallographic **a**-axis; AFM = antiferromagnetic spin arrangement

interaction. However, an exception to this phenomenological rules has been reported for $NaCrGe_2O_6$, space group $C2/c$. This pyroxene shows even larger Cr–O1–Cr angles of 101.2(1)° (Redhammer et al. 2008), but has a pure ferromagnetic ordering of spins, both within and between the M1 chains (Nenert et al. 2009a). Major differences between the sodium and Li compound beyond the different space group symmetry are the larger Cr–Cr distances, both within (3.140(1) Å) and especially between different M1 chains in $NaCrGe_2O_6$. Here, the shortest distances are 5.666(1) and 6.643(1) Å, being significantly larger than the shortest Cr–Cr contact between M1 chains in $LiCrGe_2O_6$, respectively (see above). Obviously, the small structural adjustments (increasing Cr–Cr distances) lead to a change in the magnetic ground state from ferromagnetic ($NaCrGe_2O_6$) to pure antiferromagnetic ($LiCrGe_2O_6$). While $NaCrGe_2O_6$ is different, the silicate $LiCrSi_2O_6$ (mineral name kosmochlore), which also has space group $P2_1/c$ at low temperatures (Redhammer and Roth 2004a), has a remarkably similar magnetic spin structure to $LiCrGe_2O_6$. The magnetic space group of $LiCrSi_2O_6$ was determined to be $P2_1'/c$; the spins are oriented within the **a**–**c** plane and form an angle of 31.9(1)° with the crystallographic **a**-axis (Nenert et al. 2010b). A major difference between these two structures is a reduced magnetic moment of moment $\mu(Cr^{3+}) = 2.06(4)$ μB. This was recently interpreted by different numbers of exchange integrals in $LiCr(Si,Ge)_2O_6$ by Janson et al. (2014).

$LiFeGe_2O_6$, which has M1–$M1_{intra}$ distances similar to those in $LiCrGe_2O_6$ with values of 5.420(2) and 5.544(2) Å, respectively, at 5 K, displays the same magnetic space group as $LiCrGe_2O_6$ ($P2_1'/c$), but has a more complex spin structure with a doubling of the a lattice parameter. This is the result of the different intra-chain couplings, which depend on the nature of the superexchange pathway: $[Fe–Fe]_{inter}$ coupling via the GeA tetrahedron is ferromagnetic, while the coupling via the GeB tetrahedron is antiferromagnetic. As mentioned above, in $LiCrGe_2O_6$ the spins are oriented within the **a**–**c** plane with a neglecting component along the **b**-axis, forming an angle of 30.5(2)° with the crystallographic **a**-axis at 0.5 K. There is no evident change in spin orientation between 0.5 and 5 K; only the data at 6 K suggest some lower value shortly after the onset of magnetic ordering. The spin orientation is another distinct difference to $NaCrGe_2O_6$, where the spins are oriented along the **c**-axis only. The variation in the magnetic moment with temperature in $LiCrGe_2O_6$ is displayed in Fig. 11. With decreasing T, the total magnetic moment increases, following a power law according to $M(T) = M(0)*[1 - (T/T_N)^{\alpha}]^{\beta}$ with $M(0) = 2.36$, $T_N = 6.3$ K, and $\alpha = 2.46$. The critical exponent $\beta = 0.31$ is close to the values to be expected for a 3D Heisenberg or Ising model for the magnetic ordering. Around 2 K, a maximum value of $\mu(Cr^{3+}) = 2.34(6)$ μ_B is reached, which is close to the expected spin-only theoretical value of $\mu(Cr^{3+}) = 2.50$ μ_B. However, below this temperature, $M_{(total)}$ is decreasing again toward 1 K. As we obtain the same values of $\mu(Cr^{3+})$ at 2 K as was obtained by Nenert et al. (2010b), we assume this effect to be real. The lattice parameters also show discontinuities around 1 K. No additional magnetic peaks arise, which could hint a change in magnetic symmetry. Most probably, this is a sign for an additional spin canting at very low temperature, which we cannot resolve with powder diffraction data, but which may be determined by single-crystal neutron diffraction.

Concluding, $LiCrGe_2O_6$ has a pure antiferromagnetic pattern of ordering at low temperature; the sodium compound—however—is fully ferromagnetic. One major difference between these two compounds is the space group with the latter displaying $C2/c$ symmetry down to lowest temperatures of 1.7 K (Nenert et al. 2009a). The role of space group symmetry (and connected to this the symmetry

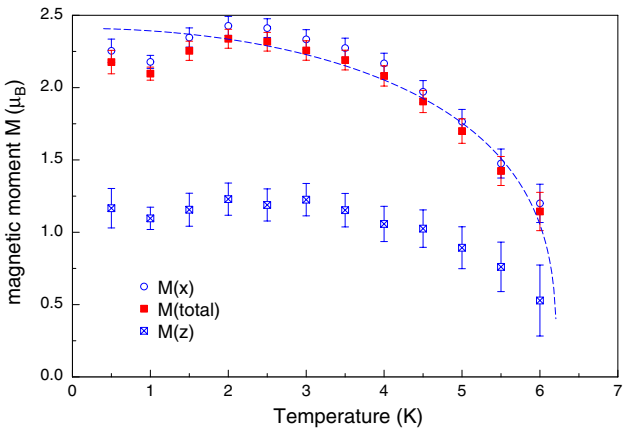

Fig. 11 Variation in the components and the total magnetic moment M in $LiCrGe_2O_6$ as a function of temperature; the curve corresponds to a fit to the data using a power law following Blundell et al. (2003)

restrains on bond length and angle variation with temperature) on the magnetic structure has not been investigated in detail in pyroxenes, but may play an important role in determining the magnetic ground state. However, this certainly is not the only factor as shown by the comparison between $LiFeGe_2O_6$ and $LiCrGe_2O_6$: Both have $P2_1/c$ symmetry, but the magnetic structure of $LiFeGe_2O_6$ is more complex as is the one of $LiCrGe_2O_6$. This is true even if the general topology of the structure is quite similar. Based on the findings of this study, structural investigations along the (Na,Li)$CrGe_2O_6$ and Li(Cr,Fe)Ge_2O_6 solid solution series would be of great interest to obtain a better insight into the structural features that determine the magnetic ground state. An additional interesting finding is the observation of a shift in Cr atoms within the equatorial plane of the octahedron in the vicinity of the magnetic ordering temperature. This could be a direct evidence for some kind of (ferroelectric/elastic) dipole distortion at the magnetic phase transition, an effect which should be looked onto in more detail, not only in $LiCrGe_2O_6$ but in the magnetic pyroxenes in general.

Acknowledgments Neutron diffraction experiments have been supported by the European Commission under the 7th Framework Programme through the "Research Infrastructures" action of the "Capacities" Programme, Contract No: CP_CSA_Infra-2008-1.1.1 Number 226507-NIMI3.

References

Angel R (2011) Win_Strain 4.11. http://www.rossangel.com/home.htm

Bertaut EF (1968) Representation analysis of magnetic structures. Acta Crystallogr A A24:217–231

Blundell SJ, Steer CA, Pratt FL, Marshall IM, Hayes W, Ward RCC (2003) Detection of magnetic order in the S = 1 chain compound $LiVGe_2O_6$ using implanted spin-polarized muons. Phys Rev 67:224411

Cámara F, Iezzi G, Oberti R (2003a) HT-XRD study of synthetic ferrian magnesian spodumene: the effect of site dimension on the $P2_1/c \leftrightarrow C2/c$ phase transition. Phys Chem Miner 30:20–30

Cámara F, Carpenter MA, Domeneghetti MC, Tazzoli V (2003b) Coupling between non-convergent ordering and transition temperature in the $C2/c \leftrightarrow P2_1/c$ phase transition in pigeonite. Am Mineral 88:1115–1128

Cámara F, Nestola F, Angel RJ, Ohashi H (2009) Spontaneous strain variations through the low-temperature displacive phase transition of $LiGaSi_2O_6$ clinoyproxene. Eur J Mineral 21:599–614

Goodenough JB (1963) Magnetism and the chemical bond. Wiley, New York

Hoelzel M, Senyhyn A, Gilles R, Boysen H, Fuess H (2007) The structure powder diffractometer SPODI. Neutron News 18(4):23–26

Janson O, Nénert G, Isobe M, Skourski Y, Ueda Y, Rosner H, Tsirlin AA (2014) Magnetic pyroxenes $LiCrGe_2O_6$ and $LiCrSi_2O_6$: dimensionality crossover in a non-frustrated S = 3/2 Heisenberg model. arXiv:1402.5054v1

Jodlauk S, Becker P, Mydosh JA, Khomskii DI, Lorenz T, Streltsov SV, Hezel DC, Bohaty L (2007) Pyroxenes: a new class of multiferroics. J Phys Condens Matters 19(43):432201

Knight KS (1996) A neutron powder diffraction determination of the thermal expansion tensor of crocoite ($PbCrO_4$) between 60 K and 290 K. Mineral Mag 60:963–972

Litvin DB (2008) Tables of crystallographic properties of magnetic space groups. Acta Crystallogr A 64:419–424

Matsushita Y, Izumi F, Isobe M, Ueda Y (2010) Crystal structures of Cr-based magnetic pyroxenes. Solid State Sci 12(5):676–679

Nenert G, Ritter C, Isobe M, Isnard O, Vasiliev AN, Ueda Y (2009a) Magnetic and crystal structures of the one-dimensional ferromagnetic chain pyroxene $NaCrGe_2O_6$. Phys Rev B 80:024402

Nenert G, Isobe M, Ritter C, Isnard O, Vasiliev AN, Ueda Y (2009b) Magnetic and crystal structures of the magnetoelectric pyroxene $LiCrSi_2O_6$. Phys Rev B 79:064416

Nenert G, Kim I, Isobe M, Ritter C, Vasiliev AN, Kim KH, Ueda Y (2010a) Magnetic and magnetoelectric study of pyroxene $NaCrSi_2O_6$. Phys Rev B81:184408

Nenert G, Isobe M, Kim I, Ritter C, Colin CV, Vasiliev AN, Kim KH, Ueda Y (2010b) Interplay between low dimensionality and magnetic frustration in the magnetoelectric pyroxenes $LiCrX_2O_6$ (X = Ge, Si). Phys Rev B 82:024429

Nestola F, Boffa Ballaran T, Ohashi H (2008) The high-pressure $C2/c$–$P2_1/c$ phase transition along the $LiAlSi_2O_6$–$LiGaSi_2O_6$ solid solution. Phys Chem Miner 35:477–484

Nestola F, Redhammer GJ, Pamato MG, Secco L, Dal Negro A (2009) High-pressure phase transformation in $LiFeGe_2O_6$ pyroxene. Am Mineral 94:616–621

Ohashi Y, Burnham CW (1973) Clinopyroxene lattice deformations: the roles of chemical substitutions and temperature. Am Mineral 58:843–849

Prencipe M, Tribaudino M, Pavese M, Hoser A, Reehuis M (2000) A single-crystal neutron-diffraction investigation of diopside at 10 K. Can Mineral 38:183–189

Redhammer GJ, Roth G (2004a) Structural changes upon the temperature dependent $C2/c \rightarrow P2_1/c$ phase transition in $LiMe^{3+}Si2O6$ clinopyroxenes, Me = Cr, Ga, Fe, V and Sc. Zeitschrift für Kristallographie 219(10):585–605

Redhammer GJ, Roth G (2004b) Structural variation and crystal chemistry of $LiMe^{3+}Si_2O_6$ clinopyroxenes, Me^{3+} = Al, Ga, Cr, V, Fe, Sc and In. Z Kristallogr 219:278–294

Redhammer GJ, Roth G, Paulus W, André G, Lottermoser W, Amthauer G, Treutmann W, Koppelhuber-Bitschnau B (2001) Crystal and magnetic structure of Li-aegirine $LiFe^{3+}Si_2O_6$: a temperature dependent study. Phys Chem Miner 28:337–346

Redhammer GJ, Roth G, Ohashi H (2003) Single crystal structure refinement of $NaTiSi_2O_6$ clinopyroxene at low temperatures (100 K < T < 298 K). Acta Crystallogr A B59:730–746

Redhammer GJ, Roth G, Treutmann W, Paulus W, André G, Pietzonka C, Amthauer G (2008) Magnetic ordering and spin structure in Ca-bearing clinopyroxenes $CaM^{2+}(Si, Ge)_2O_6$, M = Fe, Ni Co, Mn. J Solid State Chem 181:3163–3176

Redhammer GJ, Roth G, Amthauer G (2009a) Chromium-based clinopyroxene-type germanates $NaCrGe_2O_6$ and $LiCrGe_2O_6$ at 298 K. Acta Crystallogr A C64:i97–i102

Redhammer GJ, Roth G, Treutmann W, Hoelzel M, Paulus W, André G, Pietzonka C, Amthauer G (2009b) The magnetic structure of clinopyroxene-type $LiFeGe_2O_6$ and revised data on multiferroic $LiFeSi_2O_6$. J Solid State Chem 182:2374–2384

Redhammer GJ, Senyshin A, Tippelt G, Pietzonka C, Roth G, Amthauer G (2010a) Magnetic and nuclear structure and thermal expansion of orthorhombic and monoclinic polymorphs of $CoGeO_3$ pyroxene. Phys Chem Miner 37(5):311–332

Redhammer GJ, Cámara F, Alvaro M, Nestola F, Tippelt G, Prinz S, Simons J, Roth G, Amthauer G (2010b) Thermal expansion and high temperature $P2_1/c$–$C2/c$ phase transition in clinopyroxene-type $LiFeGe_2O_6$ and comparison to $NaFe(Si, Ge)_2O_6$. Phys Chem Miner 37:685–704

Redhammer GJ, Senyshyn A, Meven M, Roth G, Prinz S, Pachler A, Tippelt G, Piezonka C, Treutmann W, Hoelzel M, Pedersen B, Amthauer G (2011a) Nuclear and incommensurate magnetic structure of $NaFeGe_2O_6$ between 5 K and 298 K and some comparison to $NaFeSi_2O_6$. Phys Chem Miner 38:139–157

Redhammer GJ, Senyshyn A, Tippelt G, Roth G (2011b) Magnetic spin structure of pyroxene-type MnGeO3. J Phys Condens Matter 23:254202

Redhammer GJ, Senyshyn A, Tippelt G, Pietzonka C, Treutmann W, Roth G, Amthauer G (2012) Magnetic and low temperature structural behavior of clinopyroxene-type $FeGeO_3$: a neutron diffraction, magnetic susceptibility and ^{57}Fe Mössbauer study. Am Mineral 97(3):694–706

Redhammer GJ, Roth G, Senyshyn A, Tippelt G, Pietzonka C (2013) Crystal and magnetic spin structure of Germanium–Hedenbergite, $CaFeGe_2O_6$, and a comparison with other magnetic/magnetoelectric/multiferroic pyroxenes. Z Kristallogr 228(3):140–150

Rodríguez-Carvajal J (2001) Recent developments of the program. In: Commission on powder diffraction (IUCr). Newsletter 26:12–19. http://journals.iucr.org/iucr-top/comm/cpd/Newsletters/

Schlenker JL, Gibbs GV, Boisen MB Jr (1975) Thermal expansion coefficients for monoclinic crystals: a phenomenological approach. Am Mineral 60:828–833

Schonfield PF, Knight KS, van der Houwen JAM, Valsami-Jones E (2004) The role of hydrogen bonding in the thermal expansion and dehydration of brushite, di-calcium phosphate dihydrate. Phys Chem Miner 31:606–624

Shannon RD, Prewitt CT (1969) Effective ionic radii in oxides and fluorides. Acta Crystallogr A B25:925–946

Streltsov SV, Khomskii DI (2008) Electronic structure and magnetic properties of pyroxenes (Li, Na)TM(Si, Ge)$_2O_6$: low-dimensional magnets with 90° bonds. Phys Rev B 77:064405

Tribaudino M, Mantovani L (2014) Thermal expansion in *C*2/*c* pyroxenes: a review and new high-temperature structural data for a pyroxene of composition $(Na_{0.53}Ca_{0.47})(Al_{0.53}Fe_{0.47})Si_2O_6$ ($Jd_{53}Hd_{47}$). Mineral Mag 78(2):311–324

Tribaudino M, Nestola F, Cámara F, Domeneghetti MC (2002) The high-temperature $P2_1/c \leftrightarrow C2/c$ phase transition in Fe-free pyroxene ($Ca_{0.15}Mg_{1.85}Si_2O_6$): structural and thermodynamic behavior. Am Mineral 87:648–657

Tribaudino M, Nestola F, Meneghini C, Bromiley GD (2003) The high-temperature P2/c$_1$–C2/c phase transition in Fe-free Ca-rich P2$_1$/c clinopyroxenes. Phys Chem Miner 30:27–535

Tribaudino M, Bromiley G, Ohashi H, Nestola F (2009) Synthesis, TEM characterization and thermal behavior of $LiNiSi_2O_6$ pyroxene. Phys Chem Miner 36:527–536

Willis BTM, Pyror AW (1975) Thermal vibrations in crystallography, vol 1. Cambridge University Press, Cambridge